

# Model of energy spectrum parameters of ground level enhancement events in solar cycle 23

S.-S. Wu<sup>1,2</sup>, G. Qin<sup>3</sup>

<sup>1</sup>State Key Laboratory of Space Weather, National Space Science Center, Chinese Academy of Sciences, Beijing 100190,

China

<sup>2</sup>College of Earth Sciences, University of Chinese Academy of Sciences, Beijing 100049, China

<sup>3</sup>School of Science, Harbin Institute of Technology, Shenzhen, 518055, China

## Key Points:

- Study of GLE energy spectrum parameters with conditions of the corresponding solar events
- Using solar conditions to determine whether there is strong interplanetary shock acceleration
- Preliminary prediction model of energy spectrum of ground level enhancement events

---

Corresponding author: G. Qin, qingang@hit.edu.cn

## Abstract

Mewaldt et al. 2012 fitted the observations of the ground level enhancement (GLE) events during solar cycle 23 to the double power-law equation to obtain the four spectral parameters, the normalization constant  $C$ , low-energy power-law slope  $\gamma_1$ , high-energy power-law slope  $\gamma_2$ , and break energy  $E_0$ . There are 16 GLEs from which we select 13 for study by excluding some events with complicated situation. We analyze the four parameters with conditions of the corresponding solar events. According to solar event conditions we divide the GLEs into two groups, one with strong acceleration by interplanetary (IP) shocks and another one without strong acceleration. By fitting the four parameters with solar event conditions we obtain models of the parameters for the two groups of GLEs separately. Therefore, we establish a model of energy spectrum of solar cycle 23 GLEs which may be used in prediction in the future.

## 1 Introduction

Ground level enhancement (GLE) events are large solar energetic particle (SEP) events in which GeV particles are able to reach the Earth's atmosphere and produce secondary particles with intensities above the background level that is produced by the galactic cosmic rays (GCRs) so that the counts of ground-based neutron monitors (NMs) are enhanced [e.g., Reames, 1999; Lopate, 2006]. There are many studies on GLEs which can cause serious space weather effects [e.g., Shea and Smart, 2012]. Particularly in the solar cycle 23, there were even more GLE studies than previous periods because of more spacecraft in orbit, including NASA's SAMPEX, ACE, STEREO and NOAA's GOES series, onboard which the instruments extended the measurements of protons in energy  $\sim 0.1$  to  $\sim 500\text{--}700$  MeV [Mewaldt et al., 2012]. In addition, SOHO and Wind spacecraft provided important observations for GLE study in solar cycle 23, i.e., the Large Angle and Spectrometric Coronagraph (LASCO) [Brueckner et al., 1995] onboard SOHO to provide the coronal images [e.g., Gopalswamy et al., 2010] and the Radio and Plasma Wave (WAVES) experiment [Bougeret et al., 1995] onboard Wind to provide the GLE associated radio dynamic spectra in the decameter-hectometric (DH) wavelengths [e.g., Gopalswamy et al., 2010]. Furthermore, the mass and kinetic energy of coronal mass ejections (CMEs) can be provided by the CME brightness obtained from LASCO observations [e.g., Vourlidas et al., 2000; Subramanian and Vourlidas, 2007], so that one can determine the strength of shock driver. The frequency of DH type II bursts from WAVES reflects the distance between interplanetary (IP) shock and the Sun

[e.g., *Gopalswamy, 2006*], so that higher starting frequency indicates that the shock starts to accelerate particles closer to the Sun with stronger effects. It is also indicated that lower ending frequency shows that shock acceleration continues to larger distances from the Sun, which suggests a strong shock. Furthermore, the composition data from the Solar Isotope Spectrometer (SIS) [*Stone et al., 1998*] onboard ACE spacecraft can be used to determine the source of SEPs. For example, if the Fe/O ratio is higher, the SEPs are considered from flare material instead of the shock acceleration from solar wind or coronal materials [e.g., *Reames, 1999; Cane et al., 2003, 2006*].

Some research has been done to study the GLEs detected in solar cycle 23, of which some work focused on individual events separately [e.g., *Bieber et al., 2002, 2004, 2005, 2013; Grechnev et al., 2008; McCracken et al., 2008; Firoz et al., 2012*], but others systematically focused on the total GLEs [e.g., *Reames, 2009; Gopalswamy et al., 2010, 2012; Mewaldt et al., 2012*]. *Gopalswamy et al.* [2010] studied the flare and CME properties, they found that the median value of flares associated with those GLEs except GLE61 is X3.8, which is far greater than that of all flares of solar cycle 23. For GLE61, though the flare occurred behind the west limb and the associated flare value is not determined, there might have a large flare because the associated CME was exceptionally fast (2465 km/s in sky plane and 2712 km/s deprojected). *Gopalswamy et al.* [2010] also found that the average speed of GLE associated CMEs during solar cycle 23 was as large as 1916 km/s in the sky plane. Note that there was no CME observation for GLE58 when SOHO was temporarily disabled. What's more, they found that every GLE event was accompanied by a DH type II burst, which indicates strong shock [*Gopalswamy, 2006*]. *Gopalswamy et al.* [2012] is the enhanced version of *Gopalswamy et al.* [2010], and they given more information about the GLE associated flares and CMEs in solar cycle 23. What's more, they discussed the height of CMEs at solar particle release (SPR) time in detail, which was compared with the work of *Reames* [2009].

Based on the extended measurements of energetic protons from spacecraft, *Mewaldt et al.* [2012] tested three spectral forms for fitting proton energy spectra of GLEs during solar cycle 23. They found that the GLE spectra are best fitted by the double power-law shape of *Band et al.* [1993] rather than the Bessel function shape of *Ramaty* [1979] and the power-law with exponential-tail shape of *Ellison and Ramaty* [1985]. The equation of the double power-

law is given by:

$$dJ/dE = \begin{cases} C (E/E_{\text{MeV}})^{\gamma_1} \exp(-E/E_0) & \text{for } E \leq \Delta\gamma E_0 \\ C_1 (E/E_{\text{MeV}})^{\gamma_2} & \text{for } E \geq \Delta\gamma E_0, \end{cases} \quad (1)$$

where

$$\Delta\gamma = \gamma_1 - \gamma_2,$$

$$C_1 = C (\Delta\gamma E_0/E_{\text{MeV}})^{\Delta\gamma} \exp(-\Delta\gamma),$$

$$E_{\text{MeV}} = 1 \text{ MeV},$$

where  $J$  is fluence, and  $E$  is kinetic energy per nucleon. It is noted that there are four parameters in the double power-law Equation (1), namely, normalization constant  $C$ , low-energy power-law slope  $\gamma_1$ , high-energy power-law slope  $\gamma_2$ , and break energy  $E_0$ . Since  $E_0 \gg E_{\text{MeV}}$ ,  $C$  is approximately equal to the spectrum value at  $E = E_{\text{MeV}}$ . The double power-law is a piecewise function, and the demarcation point is  $\Delta\gamma E_0$ , which is called transition energy [e.g., *Mewaldt et al.*, 2012]. If the maximum energy of measurements is less than transition energy, the spectrum can be fitted just using the upper expression of Equation (1), which is the Ellison-Ramaty form. However, since there were spacecraft measurements of extended energy channels available, it is possible for one to determine which formula to be appropriate.

The probable causes of spectral shape are suggested as the shock acceleration [e.g., *Cohen et al.*, 2005; *Li et al.*, 2009; *Tylka et al.*, 2005; *Tylka and Lee*, 2006] or transport effect [e.g., *Li and Lee*, 2015; *Zhao et al.*, 2016]. *Li and Lee* [2015] studied the double power-law shape of GLEs in solar cycle 23 and obtained the analytical solution of the energy spectrum from the Parker diffusion equation with some assumptions. They found that the spectral shape of nine western GLEs are due to the scatter-dominated transport effect, while diffusive shock acceleration in IP space plays an important role in other near-central meridian GLEs. On the other hand, by only considering energetic particles' transport effects, *Zhao et al.* [2016] adopted a simulation model for energetic particles to study the formation of double power-law spectra. With the spectrum of magnetic turbulence including only the inertial range, they obtained a double power-law spectrum at 1 AU by assuming a power-law source spectrum at the Sun, and they found that the harder the power-law slope of turbulence is, the harder the low-energy power-law slope  $\gamma_1$  is and the smaller the break energy  $E_0$  is. They also suggested that including the energy-containing range the break energy  $E_0$  can be

decreased, and the smaller the correlation length in the turbulence spectrum is, the lower the break energy  $E_0$  is.

It is convenient to use the double power-law with the form in Equation (1) for the model of SEP energy spectra since there are only four parameters needed. *Mewaldt et al.* [2012] studied the fitted parameters, i.e.,  $C$ ,  $\gamma_1$ ,  $\gamma_2$ , and  $E_0$ , of the double power-law model by comparing the results from the 16 GLEs and 22 large non-GLE events during solar cycle 23. They found that  $\gamma_1$  of GLEs is usually similar to that of typical large SEP events, while  $\gamma_2$  of GLEs is harder than that of typical large SEP events. They also found that  $E_0$  of GLEs is usually in the range of  $\sim 2$  to 46 MeV.

In this paper we analyze the spectral parameters of GLEs during solar cycle 23 with conditions of the corresponding solar events to obtain models of the parameters, thus the energy spectra of GLEs can be provided which may be used for prediction. In Section 2, we introduce some observation characteristics of the intensity-time profiles of various energy protons and make the data selection. In Section 3, we show the classification of the selected GLEs. In Section 4, we present the correlations of spectral parameters with each other and solar activity. In Section 5, we obtain the statistical expressions of  $C$ ,  $\gamma_1$ ,  $\gamma_2$  and  $E_0$ , with which we establish a prediction model of energy spectrum of GLEs. In section 6, the modeling results are compared with observations for six GLEs from solar cycle 22 and one GLE from solar cycle 24. Finally, we present conclusions and discussion in Section 7.

## 2 Observations and Data Selection

In a GLE event, large amount of energetic particles are accelerated near the solar surface or in the IP space, and they are consequently transported in the heliosphere. The energetic particles can be measured at 1 AU by several spacecraft simultaneously, such as ACE, GOES, SAMPEX and STEREO missions. In Figures 1 and 2, we show the proton intensity-time profiles for the sixteen GLEs during solar cycle 23 from the Electron, Proton, and Alpha Monitor (EPAM) [*Gold et al.*, 1998] on ACE and Energetic Particle Sensor (EPS) [*Onsager et al.*, 1996] on GOES-8 or GOES-11. For GLE58, the fourth GLE in solar cycle 23 in the panel of the second row and the second column of Figure 1, there was an X1.0 class flare that began at 21:50 UT on August 24, 1998 indicated by a red vertical dashed line, and the measurements had an impulsive enhancement after tens of minutes. When an IP shock arrived at 1 AU indicated by a blue vertical dashed line, there was another enhance-

ment of proton intensities, which is called energetic storm particle (ESP) event [e.g., *Rao et al.*, 1968]. The ESP event can significantly increase the intensity of low energy protons (typically up to tens of MeVs in GLEs) with the peak intensity higher than that caused by a flare or a corona shock. However, ESP event usually has little influence on high energy protons, such as tens to hundreds MeV protons. In general, the CME originated near central meridian associates with strong ESP event. For example, with the small longitude, GLE58 and GLE59 had strong ESP events, while GLE60 and GLE61, which had large longitude, were hardly affected by the IP shock. The proton intensity-time profiles at 1 AU lasts at least two days for a GLE event, during which if an IP shock, in addition to the GLE associated one, corresponding to an earlier solar eruption arrives at 1 AU, the proton intensities would be influenced by the additional IP shock. For example, in the upper left panel of Figure 1, GLE55 associated with an X9.4 class flare that began at 11:49 UT on November 6, 1997, and the arrival of the first shock was at 22:02 UT on the same day, which was less than 12 hours later than the flare, thus we consider the shock is not corresponding to the solar event of GLE55. The upper right panel of Figure 1 exhibits the intensity-time profiles of GLE56 with an X1.1 class flare that erupted at 13:31 UT on May 2, 1998, and the arrival of the corresponding IP shock was at 17:00 UT on 3 May. In addition to the associated IP shock, there was a large forward-traveling wave arriving at 02:15 UT on 4 May indicated by the black vertical dashed line, which significantly affected the low energy proton intensities, such as particles with energy less than 10 MeV. Thus the energy spectra of GLE55 and GLE56 are influenced, which may be the reason why their break energy  $E_0$  are much bigger than that of other GLEs. The panel of the third row and the second column of Figure 2 shows the intensity-time profiles for GLE68, and there was an X3.8 class flare that erupted at 09:38 UT on January 17, 2005, but without the event associated IP shock at 1 AU. However, it is shown that about 2 hours before the solar flare associated with GLE68, an IP shock associated with a previous solar event arrived at 1 AU, and we can find that the low energy proton intensity-time profiles were affected by previous events. It can be shown that all of the GLEs except GLE68 in solar cycle 23 had a corresponding IP shock at 1 AU. Therefore, the energy spectra of GLE55, GLE56, and GLE68 are not usual comparing to other GLEs in solar cycle 23, for simplicity purpose, we exclude the three GLEs for further analysis. However, if the additional IP shock is weak, the intensity-time profiles may not be influenced significantly. Such as GLE62 in the lower right panel of Figure 1, which shows that there were three IP shocks, and the second IP shock corresponding to GLE62 associated with a strong ESP

event, while the other two shocks had little effects on the proton intensities. The above flare onset times and classes are from *Gopalswamy et al.* [2012], and the shock and wave information can be found in web ([http://www-ssg.sr.unh.edu/mag/ace/ACElists/obs\\_list.html#shocks](http://www-ssg.sr.unh.edu/mag/ace/ACElists/obs_list.html#shocks), <https://www.cfa.harvard.edu/shocks>).

Energy spectrum can be obtained by integrating the proton intensity-time profiles observed by spacecraft near the Earth. Figure 3 shows the energy spectrum of a typical GLE with the four spectral parameters. Note that, the value of normalization constant  $C$  does not affect the shape of spectrum, but it controls the level of energy spectrum. Low-energy slope  $\gamma_1$  is always affected by the ESP event especially when the shock nose is nearly toward the Earth, because ESP event can significantly enhance the low energy proton intensities. It is assumed that high-energy slope  $\gamma_2$  can be influenced only by a very strong toward-Earth IP shock.

In this work, the four spectral parameters of GLEs during solar cycle 23 are obtained by *Mewaldt et al.* [2012]. The flare locations listed in Table 1 associated to these GLEs are also from *Mewaldt et al.* [2012]. The longitude of the flares range from E09 to W117, and the asymmetry of longitude is caused by the transport of SEPs in the Parker spiral field. Some other related parameters that would be used in the following sections are also listed in Table 1. In this work we would analyze the four spectral parameters depending on the event conditions for the 13 selected GLEs in solar cycle 23.

### 3 Classification of Events

Since strong IP shock acceleration of energetic particles for a GLE can enhance the low energy part of energy spectrum significantly, the high-energy power-law slope  $\gamma_2$  would become smaller [see, e.g., Figure 13 of *Mewaldt et al.*, 2012]. Figure 4 shows  $\gamma_2$  as a function of the flare longitude  $\theta$ . The numbers in the figure indicate the GLE number. We set threshold values  $\theta_t = W40$  and  $\gamma_{2t} = -3.6$ . The vertical dashed line,  $\theta = \theta_t$  divides all events into two parts. We assume that  $\theta \leq \theta_t$  and  $\theta > \theta_t$  indicate the IP shock nose being nearly toward the Earth and not toward the Earth, respectively. In addition, the horizontal dashed line,  $\gamma_2 = \gamma_{2t}$ , divides all events into green and blue categories. From Figures 1 and 2, we find that for the green events the peak intensity of  $\sim 60$  MeV protons caused by ESP event,  $P_E$ , is higher than that caused by flare or coronal shock,  $P_C$ , or  $P_E > P_C$ ; While  $P_E < P_C$  for the blue events. Therefore, we assume that green ( $\gamma_2 \leq \gamma_{2t}$ ) and blue ( $\gamma_2 > \gamma_{2t}$ ) events indicate

strong and weak IP shock acceleration, respectively. From Figure 4 we can see that all the events with IP shocks being not toward the Earth have weak IP shock acceleration. However, if the IP shock nose is toward the Earth, the events could be either in green or blue category. We assume generally a green event corresponds to a strong solar eruption. Therefore, it is possible we use other solar event conditions to distinguish between the green and blue events if the shock nose is toward the Earth.

Firstly, the brightness of CME image can be used to distinguish between the blue and green events if the shock nose is toward the Earth. The white light image of CME can be obtained from the LASCO onboard SOHO. The main steps are as follows. First, we select a sequence of images which recorded the evolution of a CME and a pre-event image from the LASCO/C2 field of view and convert them to gray images, then use the median filtering algorithm [e.g., *Shen and Qin, 2016*] to get the so called "clean" images by removing their noise. Next, we make differences of the clean images between the event time ones and the pre-event one to obtain the pure CME images. Last, for each of the pure CME images we calculate the average brightness, of which we choose the largest value to denote as the brightness of CME image.

Figure 5(a) exhibits one of the gray scale CME images of GLE59, and Figure 5(b) shows the clean image by removing the noise in Figure 5(a) while Figure 5(c) is the clean image at pre-event time, and Figure 5(d), which is called the pure CME image of GLE59, is obtained by subtracting Figure 5(c) from Figure 5(b). The white circle in the figure represents the size of the Sun, and the small red circle represents the size of the occulting disk of C2. The average brightness is calculated in the area between the two red circles. Figure 6 is similar as Figure 5 except that it is for GLE70. Comparing the pure CME images of GLE59 and GLE70 we find that the brightness of CME image of GLE70 is significantly lower than that of GLE59. The brightness of CME image of the events with shock nose toward the Earth are plotted as function of  $\gamma_2$  in Figure 7, in which we denote  $\phi$  as the brightness of CME image, and it's shown that  $\phi$  of green events are larger than that of blue events. Note that GLE58, a green event, is not included in Figure 7 since there was no C2 data available for GLE58. Furthermore, we can set the threshold value  $\phi_t = 13$ . When the flare longitude  $\theta$  of a GLE is less than the threshold  $\theta_t$ ,  $\gamma_2$  would be smaller and larger than  $\gamma_{2t}$  indicating the strong and weak IP shock acceleration if  $\phi$  is larger and smaller than  $\phi_t$ , respectively. LASCO/C3 field of view can also record the evolution of CMEs, so that one can use C3 images to determine the IP shock acceleration strength similarly.



Next, we show that the starting and ending frequencies of DH type II bursts from the WAVES onboard Wind can also be used to separate the green and blue events if the shock nose is toward the Earth. In Figure 8, we show  $\gamma_2$  as a function of the starting and ending frequencies of the associated DH type II bursts, obtained by *Gopalswamy et al.* [2010], in left and right panels, respectively. It is noted that the maximum frequency of measurements is 14 MHz, so that the starting frequency of the green events are all greater than or equal to 14 MHz. We find that both the starting and ending frequencies of DH type II bursts are effective in distinguishing the blue and green events. The frequency of DH type II bursts reflects the distance between IP shock and the Sun [e.g., *Gopalswamy, 2006*], so that higher starting frequency indicates that the shock starts to accelerate particles closer to the Sun. Therefore, the green events with a shorter distance from the Sun to start accelerating may have stronger acceleration of the shock. The ending frequencies of the green events are less than that of the blue ones, it is suggested that the shock acceleration of green events continues to larger distances from the Sun. However, recognizing a DH type II burst from a dynamic spectrum might take some time, because the frequency drift rates are not very large and the bursts are often intermittent. Therefore, the starting and ending frequencies of DH type II bursts is not suitable for predicting energy spectra.

Furthermore, the event-integrated Fe/O ratio and Ne/O ratio can be used to determine the acceleration source [e.g., *Reames, 1999*]. Figure 9 shows the 12–45 MeV/nuc Fe/O ratio, obtained by *Mewaldt et al.* [2012], from ACE/SIS measurements. It is shown that for  $\theta \leq \theta_t$ , if the 12–45 MeV/nuc Fe/O ratio is smaller (larger) than 0.15,  $\gamma_2$  would be smaller (larger) than  $\gamma_{2t}$ , indicating strong (weak) IP shock acceleration. It is assumed that the high value of Fe/O ratio indicates the SEPs from flare material, while the low value indicates the SEPs from solar wind or coronal materials [e.g., *Reames, 1999; Cane et al., 2003, 2006*]. The SEPs from solar wind or coronal materials indicates stronger IP shock acceleration than that from flare material does. We can get similar results with 12–45 MeV/nuc Ne/O ratio. From the above analysis, it is shown that the 12–45 MeV/nuc Fe/O ratio and Ne/O ratio can be used to determine if the IP shock acceleration is strong or weak, the results are consistent with our previous findings. In addition, other properties such as ionization states and isotope abundances studied by *Reames* [1999] may also distinguish these events effectively. However, the composition data of an SEP event are too late for one to use for predicting energy spectra.

Therefore, one can use the brightness of CME image to distinguish between green and blue events if the shock nose is toward the Earth.

#### 4 Statistical Analysis

In order to obtain a model with good results comparing to the observations, we first try to eliminate the correlations between the spectral parameters themselves. Besides, one can also obtain physical understanding of the GLE phenomenon in this way. The cross correlations of the four spectral parameters for the thirteen selected GLEs are presented in Figure 10. Here, blue and green stand for blue and green events, respectively, and dashed lines indicate the linear fitting. The regression parameters, correlation coefficients, and the level of statistical significance of the fitting are presented in Table 2. From the cross correlations we find that only  $\gamma_1$  and  $\log E_0$  have a good correlation. Therefore, we can eliminate one parameter from  $\gamma_1$  and  $E_0$  when we establish a model of energy spectrum of GLEs.

GLEs are caused by solar eruptions, the strength of which is relevant to the solar activity. Thus, we assume that the energy spectrum is relevant to the solar activity. The 10.7 cm solar radio flux ( $F_{10.7}$ ) is one of the indices of solar activity [e.g., *Tapping*, 2013], so that  $F_{10.7}$  can be used to study the energy spectrum. Figure 11 shows the spectral parameters,  $\log E_0$  and  $\gamma_2$  for the selected GLEs in the upper and lower panels, respectively, as function of  $F_{10.7}$  which is the value for previous day from the NOAA's Space Weather Prediction Center (SWPC, <ftp://ftp.swpc.noaa.gov/pub/warehouse>). In the upper panel of Figure 11,  $E_0$  increases with the increase of  $F_{10.7}$  for both types of events, which is reasonable since energetic particles may be accelerated more efficiently if the solar activity is high. In the lower panel of Figure 11, the green and blue dashed fitting lines have the same trend, while the green and blue lines are separated with the green line is lower in the value of  $\gamma_2$  since the strong IP shock acceleration can significantly increase the intensity of low energy particles to make high-energy slope  $\gamma_2$  smaller.

Another spectral parameter, the normalization constant  $C$ , is not related to the shape of energy spectrum, but it controls the level of the energy spectrum, i.e.,  $C$  is associated with the energy spectra in 1 MeV. It is known that the low energy protons can be influenced by the IP shock, whose strength is relevant with the flare longitude  $\theta$ . Therefore,  $C$  is possibly relevant with  $\theta$ . The strength of soft X-ray burst is relevant with solar activity at the time of event [*Thomas and Teske*, 1971], and flare may also be a source of particle acceleration.

Therefore,  $C$  is assumed to be also related to  $F_{sxr}$ , which is the integral soft X-ray flux of flare and its value can be found in the NOAA's SWPC (<ftp://ftp.swpc.noaa.gov/pub/warehouse>). Note that there is no data for  $F_{sxr}$  of GLE61 which is a backside event. One may use the space speed of CME to determine the value of  $F_{sxr}$ . Figure 12 shows the relationship between  $F_{sxr}$  and CME space speed  $v_{cme}$  which is from *Gopalswamy et al.* [2012]. It is clear to see that  $\log F_{sxr}$  can be expressed as a linear function of  $v_{cme}$ ,

$$\log F_{sxr} = 3.82 \times 10^{-4} \frac{v_{cme}}{v_0} - 1.11,$$

where  $v_0 = 1$  km/s and the expression is used to calculate  $F_{sxr}$  of GLE61. Figure 13 shows that  $\log C$  is plotted versus  $\theta$  and  $\log F_{sxr}$ , from which we can see that both the blue and green events have good correlations between  $\log C$  and  $\theta$  while only blue events have a moderate correlation between  $\log C$  and  $\log F_{sxr}$ . Therefore, blue events may have a better correlation between  $\log C$  and the combination of  $\theta$  and  $\log F_{sxr}$ , such as  $\theta \cdot \log(F_{sxr}/5)$ . Choosing  $\log(F_{sxr}/5)$  instead of  $\log F_{sxr}$  can make all of the values have the same sign, so that it is easy to combine with  $\theta$  for linear fit. Figure 14 exhibits the linear fitting for  $\log C$  as a function of  $\theta$  for green events and that of  $\theta \log(F_{sxr}/5)$  for blue events in left and right panels, respectively. It is shown for both green and blue events good linear fitting can be obtained.

The values of regression parameters  $a$  and  $b$ , the correlation coefficients and the level of statistical significance are listed in Table 2.

## 5 Energy Spectrum Model for GLEs

From the results in Figures 10, 11, 14, and Table 2, the expressions of the spectral parameters are given as following:

$$E_0 = 10^{aF_{10.7}+b}, \quad (2)$$

with  $a = 0.00404$  and  $b = 0.360$  for blue events, and  $a = 0.00326$  and  $b = 0.634$  for green events;

$$\gamma_2 = aF_{10.7} + b, \quad (3)$$

with  $a = -0.00521$  and  $b = -1.78$  for blue events, and  $a = -0.00327$  and  $b = -3.47$  for green events;

$$\gamma_1 = a \log E_0 + b, \quad (4)$$

with  $a = -0.519$  and  $b = -0.579$  for blue events, and  $a = 0.655$  and  $b = -2.02$  for green events;

$$C = \begin{cases} 10^{0.0252\theta+9.08} & \text{for green events;} \\ 10^{0.0103\theta \log(F_{sxr}/5)+8.86} & \text{for blue events.} \end{cases} \quad (5)$$

The Equations (1) and (2)–(5) may be used to establish a model of energy spectrum with the flare's longitude  $\theta$ , integral soft X-ray flux  $F_{sxr}$ , and 10.7 cm solar radio flux  $F_{10.7}$  as the input. In addition, to determine the type of GLEs, the brightness of CME image of the events is also needed.

The comparison of the energy spectra between our new model and the spacecraft observations for the 13 selected GLEs during solar cycle 24 is presented in Figure 15. Here,  $\delta$  indicates the disagreement between the model and the observations defined as the following:

$$\delta = \sqrt{\frac{1}{N} \sum_{i=1}^N [\log F(E_i) - \log f(E_i)]^2}, \quad (6)$$

where  $F(E)$  and  $f(E)$  are energy spectra from the model and observations, respectively. From Figure 15 we can see that GLE57 has the biggest  $\delta$ , and the disagreement is mainly due to the fact that  $C$  from the model is not accurate relative to the observation. On the other hand, for GLE66 and GLE67, the model results of  $C$  is not accurate but the values of  $\delta$  are smaller than that for GLE57, because in addition to the not accurate  $C$  the model also provides worse parameters  $\gamma_1$  for GLE66 and  $\gamma_2$  for GLE67, and the combination of some not accurate parameters might offset each other. It is also shown that except  $\gamma_2$ , other parameters from the model for GLE69 are more accurate comparing to that for GLE67, though the values  $\delta$  for GLE67 and GLE69 are similar.

## 6 Partial Validity Check of Energy Spectrum Model

Next, to partially check its validity, we use the new model to provide the energy spectrum of other GLEs. Table 3 shows the key parameters of six GLEs in solar cycle 22, GLE40, GLE41, GLE45, GLE48, GLE52, and GLE53, and one GLE in solar cycle 24, GLE 71, as selected for this purpose. In Table 3, the first four columns are the GLE No., solar cycle No., GLE date, and flare location, respectively, which are from *Le et al.* [2013] and [*Gopalswamy et al.*, 2013] for GLEs during solar cycles 22 and 24, respectively. The last two columns are for  $F_{10.7}$  and  $F_{sxr}$ .

In solar cycle 22, there are fifteen GLEs (GLE numbers from 40 to 54), among which four GLEs are backside events so that  $F_{s,xr}$  can not be obtained. What's more, there are five events with flare longitude less than W40 whose blue or green categories can not be determined because the data used in the classification methods introduced in Section 3 are not available. The remaining events as listed in Table 3, are selected, of which the modeling spectra are calculated in Figure 16. The observations are from GOES-7 differential channels (channels P2–P6, energy ranging from 6.6 to 114 MeV, calibrated by *Sandberg et al.* [2014]). Generally, the modeling spectra agree well with the observations of the GLEs, except for the GLE40, for which the observations of intensity of low energy channels are unusually low and do not agree with the model. Figure 17 shows the intensity-time profiles for GLE40. It is shown that the intensities of the lower energy P2–P4 channels are suppressed in the first ten hours of the events, are assumed not accurate and marked in red in the upper left panel of Figure 16. The inaccuracy can be assumed to be caused by some local structure effects, e.g., magnetospheric effects, which are not very strong for protons  $> 10$  MeV normally.

Figure 18 shows, for GLE71 of solar cycle 24, the comparison between the modeling results and the observations from ACE/EPAM (energy ranging from  $\sim 0.1$  to  $\sim 3$  MeV) and GOES-13 differential channels (channels P6–P7, energy ranging from 113.3 to 178.5 MeV, calibrated by *Bruno* [2017]), and integral channels ( $> 5$ ,  $> 10$ ,  $> 30$ ,  $> 50$ ,  $> 60$ , and  $> 100$  MeV, described in *Mewaldt et al.* [2005]). It is shown that generally the modeling results agree well with observations for GLE71, except that in lower energy range the intensity from observations, marked in red, is relatively higher than that from modeling. In the intensity-time profiles exhibited in Figure 19, there are two IP shocks, first of which corresponds to an earlier event. In general, IP shocks can accelerate lower energy protons to enhance their intensity. Therefore, the intensity observations of EPAM for GLE71 are higher than the modeling results.

All in all, the modeling results exhibited in Figures 16 and 18 show that the new model can represent the data fits of the seven GLEs to a relatively good accuracy in energy ranging from  $\sim 6$  to  $\sim 100$ – $200$  MeV.

## 7 Conclusions and Discussion

In this paper, we analyze the four spectral parameters, i.e., the normalization constant  $C$ , low-energy power-law slope  $\gamma_1$ , high-energy power-law slope  $\gamma_2$ , and break energy  $E_0$ ,

which are obtained from *Mewaldt et al.* [2012] by fitting the GLE observations during solar cycle 23 to the double power-law equation. In the statistics, we exclude GLE55, GLE56, and GLE68 out of the total of 16 GLEs in solar cycle 23 for simplicity purpose, because the conditions of the three GLEs are complicated comparing to that of the rest ones. We divide the selected GLEs into two types of events according to  $\gamma_2$ , i.e., the blue and green events with large and small  $\gamma_2$ , respectively. Because large enhancement of lower energy particles from strong IP shock acceleration would decrease  $\gamma_2$ , we assume that the small  $\gamma_2$  indicates strong IP shock acceleration. We find that all the events with large longitude are blue events with large  $\gamma_2$ . But it is shown that with small longitude one need to distinguish between blue and green events. We find that the use of the brightness of CME image, the starting and ending frequencies of DH type II bursts, and the 12–45 MeV/nuc Fe/O ratio and Ne/O ratio are different between the blue and green events, so that they can be used to distinguish the blue and green events. However, to consider about the availability of the data during near the solar eruption we may choose the brightness of CME image to distinguish the two types of events with small longitude.

We find in each type of GLE events, for the spectral parameters, only  $\gamma_1$  and  $E_0$  have strong linear relationship when considering the cross correlation, and  $\gamma_2$ ,  $E_0$  are relevant with 10.7 cm solar radio flux,  $F_{10.7}$ . For the green events,  $C$  is correlated with flare longitude,  $\theta$ . While for the blue events,  $C$  has a better relationship with the combination of  $\theta$  and  $F_{sxr}$ , i.e.,  $\theta \log(F_{sxr}/5)$ , where  $F_{sxr}$  is the integral soft X-ray flux of the flare. Therefore, we obtain the expressions for the four parameters as function of solar event conditions in solar cycle 23, thus a model of energy spectrum for GLEs in the period is established. We also compare the energy spectra from model with the observed ones of solar cycle 23 GLEs. However, we can see that for the model there are cases with one inaccurate parameter resulting in large error, but there are some other cases with several inaccurate parameters without resulting in large error because the effects of inaccuracy may offset each other. It is also noted that from Table 2 we can see that three out of four computed correlations in Equations (2)–(5) for the green events fail the test of statistical significance at the usual 5% level, which might be because of the too small number, 4, of events in this category. Finally, we obtain modeling results for six GLEs of solar cycle 22 and GLE71 of solar cycle 24 to check the validity of the model, and we find that the model can give a relatively good results in energy ranging from  $\sim 6$  to  $\sim 100$ – $200$  MeV for the events with longitude greater than W40. However, due to the lack of observations in solar cycle 22, the modeling spectra of low energy part haven't been

checked. In addition, because the data needed to distinguish between green and blue categories are not available, the modeling results for small longitude events are also not checked.

*Li and Lee* [2015] found that the spectral shape of nine western GLEs are due to the scatter-dominated transport effect, while diffusive shock acceleration in IP space plays an important role in other near-central meridian GLEs. In this work, we suggest that the causes of the spectral shape for green and blue events may be different. In fact, the slopes of the green and blue events in the upper left panel of Figure 10 and the left panel of Figure 13 are opposite. For the upper left panel of Figure 10, we assume the green events undergo strong IP shock acceleration to cause  $E_0$  and  $\gamma_1$  larger, so that  $E_0$  and  $\gamma_1$  are positively correlated. For the blue events, the IP shock acceleration is weak, thus the transport effect plays an important role in the relationship between  $\gamma_1$  and  $E_0$ , which is similar to the simulation results by *Zhao et al.* [2016] who considered only the pure transport process. As we mentioned above,  $C$  is associated with the energy spectra in 1 MeV. For the green events in the left panel of Figure 13, the shock near Earth would significantly increase the intensity of 1 MeV protons when the shock nose crosses the magnetic field line connected to spacecraft, thus larger  $\theta$  indicates shock nose encountering the magnetic field line earlier with higher accelerating effects because shock strength decreases with increasing of the solar distance. For the blue events, the situation is complex since the fluence of the 1 MeV protons could be determined by transport effect. Therefore, the slopes of the green and blue events may be different.

The energy spectrum model may be helpful for the future prediction of the GLE's energy spectrum. One needs to get the inputs quickly enough after the solar eruption. In this model the value of  $F_{10.7}$  of the previous day is used, thus the input for  $F_{10.7}$  can be obtained on time. In addition, the flare longitude  $\theta$  and  $F_{sxx}$  can be obtained quickly from the solar image observed by ground-based telescopes and soft X-ray flux observed by GOES Solar X-Ray Sensor (XRS) [*Hanser and Sellers*, 1996], respectively. If the longitude is small, the brightness of CME image from SOHO/LASCO/C2 is needed to determine the type of an event. However, the brightness of CME image from SOHO/LASCO/C2 can not be obtained quickly for two reasons. Firstly, CME needs thirteen minutes to one or two hours to transport to the view of C2. Secondly, the data of C2 are delivered to the Earth via Deep Space Network (DSN) stations if there is telemetry contact, but they have to wait for several hours otherwise (see the description about the very latest SOHO images, <https://sohowww.nascom.nasa.gov/data/realtime/image-description.html>). Therefore, in order to use the energy spectrum model to predict one might have to wait as long as several hours after the solar eruption. It is important to study other

physical parameters that can help to determine the strength of IP shock acceleration if we want to be able to determine the type of event quickly after the solar event.

In order to improve the model of GLE energy spectrum, among other efforts, we need to study the transport of GLEs by comparing the spacecraft observations with the numerical modeling [e.g., *Qin et al.*, 2011, 2013; *Wang et al.*, 2012; *Qi et al.*, 2017]. When we can better understand acceleration and transport effects of energetic particles, we may be able to include the “unusual” GLEs omitted in the current GLE energy spectrum model. In addition, there are usually much more large non-GLE SEP events than GLEs in a solar cycle. Therefore, It is also essential for us to study the energy spectra for large non-GLE SEP events with the method similar to that in this work.

### Acknowledgments

This work was supported in part by grants NNSFC 41574172, NNSFC 41374177, and NNSFC 41125016. We thank the *ACE* EPAM, SWEPAM, MAG, SIS; *GOES* EPS, XRS; *SOHO* LASCO; *WIND* WAVES teams for providing the data used in this paper. The *ACE* data are provided by the ACE Science Center and the *GOES* data by the NOAA. We appreciate the availability of the *WIND* data at the Coordinated Data Analysis Web. We also acknowledge the CDAW CME catalog which is generated and maintained at the CDAW Data Center by NASA and The Catholic University of America in cooperation with the Naval Research Laboratory. *SOHO* is a project of international cooperation between ESA and NASA. We thank the anonymous referees for their extensive efforts to improve this work.

### References

- Band, D., J. Matteson, L. Ford, B. Schaefer, D. Palmer, B. Teegarden, T. Cline, M. Briggs, W. Paciasas, G. Pendleton, G. Fishman, C. Kouveliotou, C. Meegan, R. Wilson, and P. Lestrade (1993), BATSE observations of gamma-ray burst spectra. I. spectral diversity, *Astrophys. J.*, *413*, 281–292, doi:10.1086/172995.
- Bieber, J. W., W. Dröge, P. A. Evenson, R. Pyle, D. Ruffolo, U. Pinsook, P. Tooprakai, M. Rujiwarodom, T. Khumlumlert, and S. Krucker (2002), Energetic particle observations during the 2000 July 14 solar event, *Astrophys. J.*, *567*, 622–634, doi:10.1086/338246.
- Bieber, J. W., P. Evenson, W. Dröge, R. Pyle, D. Ruffolo, M. Rujiwarodom, P. Tooprakai, and T. Khumlumlert (2004), Spaceship Earth observations of the Easter 2001 solar particle event, *Astrophys. J.*, *601*, L103–L106, doi:10.1086/381801.



- Bieber, J. W., J. Clem, P. Evenson, R. Pyle, D. Ruffolo, and A. Sáiz (2005), Relativistic solar neutrons and protons on 28 October 2003, *Geophys. Res. Lett.*, *32*, L03S02, doi:10.1029/2004GL021492.
- Bieber, J. W., J. Clem, P. Evenson, R. Pyle, A. Sáiz, and D. Ruffolo (2013), Giant ground level enhancement of relativistic solar protons on 2005 January 20. I. Spaceship Earth observations, *Astrophys. J.*, *771*, 92, doi:10.1088/0004-637X/771/2/92.
- Bougeret, J.-L., M. L. Kaiser, P. J. Kellogg, R. Manning, K. Goetz, S. J. Monson, N. Monge, L. Friel, C. A. Meete, C. Perche, L. Sitruk, and S. Hoang (1995), WAVES: The radio and plasma wave investigation on the Wind spacecraft, *Space Sci. Rev.*, *71*, 231–263, doi:10.1007/BF00751331.
- Brueckner, G. E., et al. (1995), The Large Angle Spectroscopic Coronagraph (LASCO), *Sol. Phys.*, *162*, 357–402, doi:10.1007/BF00733434.
- Bruno, A. (2017), Calibration of the GOES-13/15 high energy proton detectors based on the PAMELA solar energetic particle observations, *Sp. Weather*, *15*, 1191-1202, doi:10.1002/2017SW001672.
- Cane, H. V., T. T. von Roseninge, C. M. S. Cohen, and R. A. Mewaldt (2003), Two components in major solar particle events, *Geophys. Res. Lett.*, *30*, 8017, doi:10.1029/2002GL016580.
- Cane, H. V., R. A. Mewaldt, C. M. S. Cohen, and T. T. von Roseninge (2006), Role of flares and shocks in determining solar energetic particle abundances, *J. Geophys. Res.*, *111*, A06S90, doi:10.1029/2005JA011071.
- Cohen, C. M., E. C. Stone, R. A. Mewaldt, R. A. Leske, A. C. Cummings, G. M. Mason, M. I. Desai, T. T. Von Roseninge, and M. E. Wiedenbeck (2005), Heavy ion abundances and spectra from the large solar energetic particle events of October-November 2003, *J. Geophys. Res. Sp. Phys.*, *110*, A09S16, doi:10.1029/2005JA011004.
- Ellison, D. C., and R. Ramaty (1985), Shock acceleration of electrons and ions in solar flares, *Astrophys. J.*, *298*, 400–408, doi:10.1086/163623.
- Firoz, K. A., W. Q. Gan, Y.-J. Moon, and C. LI (2012), An interpretation of the possible mechanisms of two ground-level enhancement events, *Astrophys. J.*, *758*, 119, doi:10.1088/0004-637X/758/2/119.
- Gold, R. E., S. M. Krimigis, S. E. Hawkins III, D. K. Haggerty, D. A. Lohr, E. Fiore, T. P. Armstrong, G. Holland, and L. J. Lanzerotti (1998), Electron, proton, and alpha monitor on the Advanced Composition Explorer spacecraft, *Space Sci. Rev.*, *86*, 541–562,

- doi:10.1023/A:1005088115759.
- Gopalswamy, N. (2006) Coronal mass ejections and type II radio bursts, in *Solar Eruptions and Energetic Particles*, edited by N. Gopalswamy, R. A. Mewaldt and J. Torsti, p. 207–220, American Geophysical Union, Washington, D. C.. doi:10.1029/165GM20.
- Gopalswamy, N., H. Xie, S. Yashiro, and I. Usoskin (2010), Ground level enhancement events of solar cycle 23, *Indian J. Radio Sp. Phys.*, *39*, 240–248.
- Gopalswamy, N., H. Xie, S. Yashiro, S. Akiyama, P. Mäkelä, and I. G. Usoskin (2012), Properties of ground level enhancement events and the associated solar eruptions during solar cycle 23, *Space Sci. Rev.*, *171*, 23–60, doi:10.1007/s11214-012-9890-4.
- Gopalswamy, N., H. Xie, S. Akiyama, S. Yashiro, I. G. Usoskin, and J. M. Davila (2013), The first ground level enhancement event of solar cycle 24: direct observation of shock formation and particle release heights, *Astrophys. J.*, *765*, L30, doi:10.1088/2041-8205/765/2/L30.
- Grechnev, V. V., et al. (2008), An extreme solar event of 20 January 2005: Properties of the flare and the origin of energetic particles, *Sol. Phys.*, *252*, 149–177, doi:10.1007/s11207-008-9245-1.
- Hanser, F. A., and F. B. Sellers (1996), Design and calibration of the GOES-8 solar x-ray sensor: The XRS, *Proc. SPIE*, *2812*, 344–352, doi:10.1117/12.254082.
- Le, G.-M., P. Li, H.-G. Yang, Y.-L. Chen, X.-X. Yang, and Z.-Q. Yin (2013), The properties of solar active regions responsible for ground level enhancements during solar cycles 22 and 23, *Res. Astron. Astrophys.*, *13*, 1219–1224, doi:10.1088/1674-4527/13/10/009.
- Li, G., and M. A. Lee (2015), Scatter-dominated interplanetary transport of solar energetic particles in large gradual events and the formation of double power-law differential fluence spectra of ground-level events during solar cycle 23, *Astrophys. J.*, *810*, 82, doi:10.1088/0004-637X/810/1/82.
- Li, G., G. P. Zank, O. Verkhoglyadova, R. A. Mewaldt, C. M. S. Cohen, G. M. Mason, and M. I. Desai (2009), Shock geometry and spectral breaks in large sep events, *Astrophys. J.*, *702*, 998–1004, doi:10.1088/0004-637X/702/2/998.
- Lopate, C. (2006) Fifty years of ground level solar particle event observations, in *Solar Eruptions and Energetic Particles*, edited by N. Gopalswamy, R. A. Mewaldt and J. Torsti, p. 283–296, American Geophysical Union, Washington, D. C.. doi:10.1029/165GM27.
- McCracken, K. G., H. Moraal, and P. H. Stoker (2008), Investigation of the multiple-component structure of the 20 January 2005 cosmic ray ground level enhancement, *J.*

- Geophys. Res.*, *113*, A12101, doi:10.1029/2007JA012829.
- Mewaldt, R. A., C. M. S. Cohen, A. W. Labrador, R. A. Leske, G. M. Mason, M. I. Desai, M. D. Looper, J. E. Mazur, R. S. Selesnick, and D. K. Haggerty (2005), Proton, helium, and electron spectra during the large solar particle events of October–November 2003, *J. Geophys. Res. Sp. Phys.*, *110*, A09S18, doi:10.1029/2005JA011038.
- Mewaldt, R. A., M. D. Looper, C. M. S. Cohen, D. K. Haggerty, A. W. Labrador, R. A. Leske, G. M. Mason, J. E. Mazur, and T. T. von Roseninge (2012), Energy spectra, composition, and other properties of ground-level events during solar cycle 23, *Space Sci. Rev.*, *171*, 97–120, doi:10.1007/s11214-012-9884-2.
- Onsager, T. G., R. Grubb, J. Kunches, L. Matheson, D. Speich, R. W. Zwickl, and H. Sauer (1996), Operational uses of the GOES energetic particle detectors, in *GOES-8 and Beyond*, edited by E. R. Washwell, *SPIE Conf. Proc.*, 2812, 281, Society of Photo-Optical Instrumentation Engineers, Bellingham, Wash. doi:10.1117/12.254075.
- Qi, S.-Y., G. Qin, and Y. Wang (2017), Numerical simulations of solar energetic particle event timescales associated with ICMEs, *Res. Astron. Astrophys.*, *17*, 33, doi:10.1088/1674-4527/17/4/33.
- Qin, G., H.-Q. He, and M. Zhang (2011), An effect of perpendicular diffusion on the anisotropy of solar energetic particles from unconnected sources, *Astrophys. J.*, *738*, 28, doi:10.1088/0004-637X/738/1/28.
- Qin, G., Y. Wang, M. Zhang, and S. Dalla (2013), Transport of solar energetic particles accelerated by ICME shocks: Reproducing the reservoir phenomenon, *Astrophys. J.*, *766*, 74, doi:10.1088/0004-637X/766/2/74.
- Ramaty, R. (1979), Energetic particles in solar flares, in *Particle Acceleration Mechanisms in Astrophysics*, edited by J. Arons, C. Max, and C. Mckee, p. 135–154, Am. Inst. of Phys., New York. doi:10.1063/1.32074.
- Rao, U. R., K. G. McCracken, and R. P. Bukata (1968), The acceleration of energetic particle fluxes in shock fronts in interplanetary space, *Canadian Journal of Physics*, *46*, S844–S848, doi:10.1139/p68-365.
- Reames, D. V. (1999), Particle acceleration at the sun and in the heliosphere, *Space Sci. Rev.*, *90*, 413–491, doi:10.1023/A:1005105831781.
- Reames, D. V. (2009), Solar release times of energetic particles in ground-level events, *Astrophys. J.*, *693*, 812–821, doi:10.1088/0004-637X/693/1/812.

- Sandberg, I., P. Jiggins, D. Heynderickx, and I. A. Daglis (2014), Cross calibration of NOAA GOES solar proton detectors using corrected NASA IMP-8/GME data, *Geophys. Res. Lett.*, *41*, 4435–4441, doi:10.1002/2014GL060469.
- Shea, M. A., and D. F. Smart (2012), Space weather and the ground-level solar proton events of the 23rd solar cycle, *Space Sci. Rev.*, *171*, 161–188, doi:10.1007/s11214-012-9923-z.
- Shen, Z.-N., and G. Qin (2016), A study of cosmic ray flux based on the noise in raw CCD data from solar images, *J. Geophys. Res.*, *121*, 10,712–10,727, doi:10.1002/2016JA023376.
- Stone, E. C., et al. (1998), The solar isotope spectrometer for the advanced composition explorer, *Space Sci. Rev.*, *86*, 357–408, doi:10.1023/A:1005027929871.
- Subramanian, P., and A. Vourlidas (2007), Energetics of solar coronal mass ejections, *Astron. Astrophys.*, *467*, 685–693, doi:10.1051/0004-6361:20066770.
- Tapping, K. F. (2013), The 10.7 cm solar radio flux ( $F_{10.7}$ ), *Sp. Weather*, *11*, 394–406, doi:10.1002/swe.20064.
- Thomas, R. J., and R. G. Teske (1971), Solar soft X-rays and solar activity II. soft X-ray emission during solar flares, *Sol. Phys.*, *16*, 431–453, doi:10.1007/BF00162486.
- Tylka, A. J., and M. A. Lee (2006), A model for spectral and compositional variability at high energies in large, gradual solar particle events, *Astrophys. J.*, *646*, 1319–1334, doi:10.1086/505106.
- Tylka, A. J., C. M. S. Cohen, W. F. Dietrich, M. A. Lee, C. G. MacLennan, R. A. Mewaldt, C. K. Ng, and D. V. Reames (2005), Shock geometry, seed populations, and the origin of variable elemental composition at high energies in large gradual solar particle events, *Astrophys. J.*, *625*, 474–495, doi:10.1086/429384.
- Vourlidas, A., P. Subramanian, K. P. Dere, and R. a. Howard (2000), Large-angle spectrometric coronagraph measurements of the energetics of coronal mass ejections, *Astrophys. J.*, *534*, 456–467, doi:10.1086/308747.
- Wang, Y., G. Qin, and M. Zhang (2012), Effects of perpendicular diffusion on energetic particles accelerated by the interplanetary coronal mass ejection shock, *Astrophys. J.*, *752*, 37, doi:10.1088/0004-637X/752/1/37.
- Zhao, L., M. Zhang, and H. K. Rassoul (2016), Double power laws in the event-integrated solar energetic particle spectrum, *Astrophys. J.*, *821*, 62, doi:10.3847/0004-637X/821/1/62.

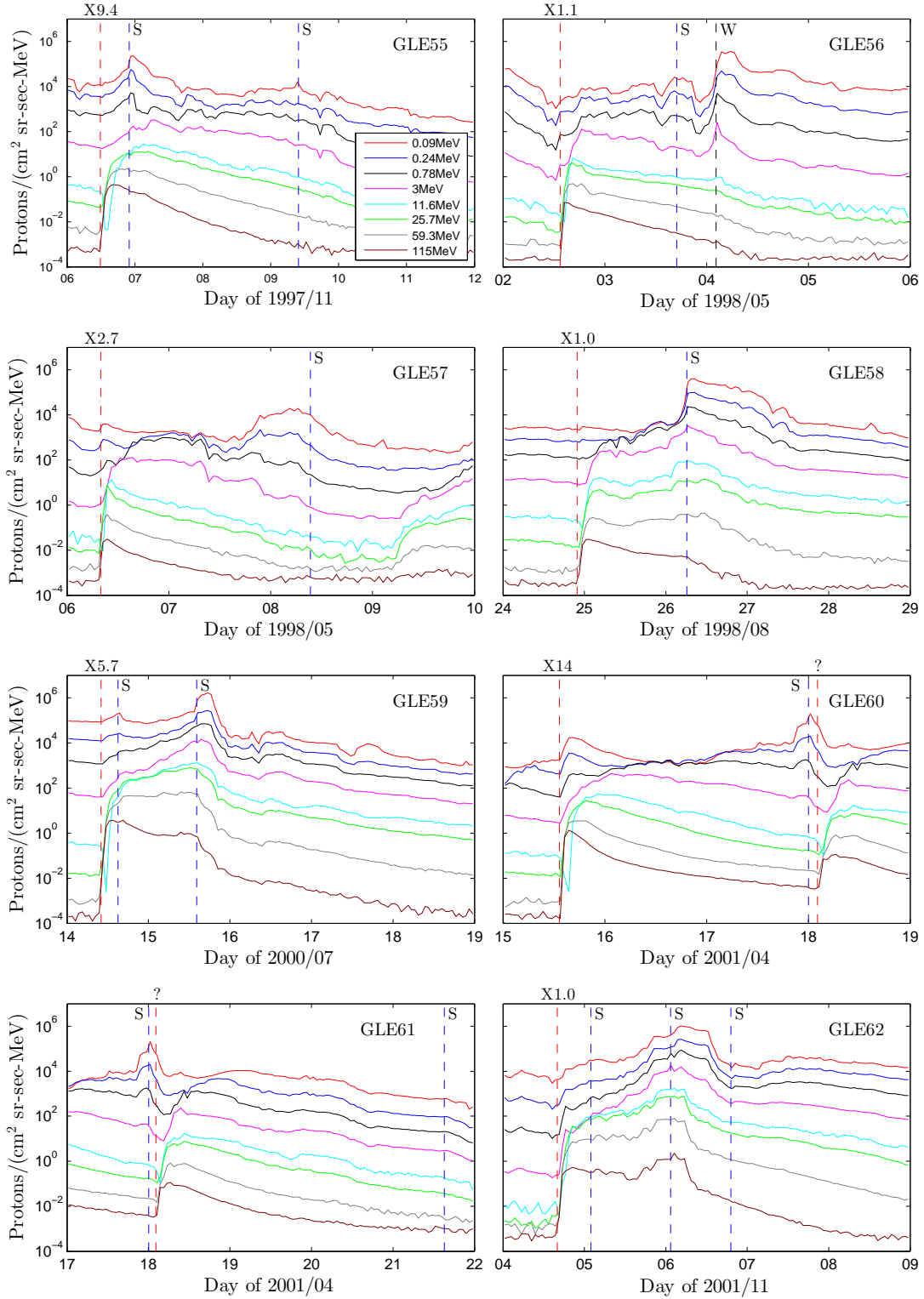


**Figure 1.** The proton intensity-time profiles for GLE55 to GLE62. The red and blue vertical dashed lines denote a solar flare eruption and an IP shock arrival at 1 AU, respectively. The black vertical dashed line in the upper right panel denotes a forward-traveling wave.

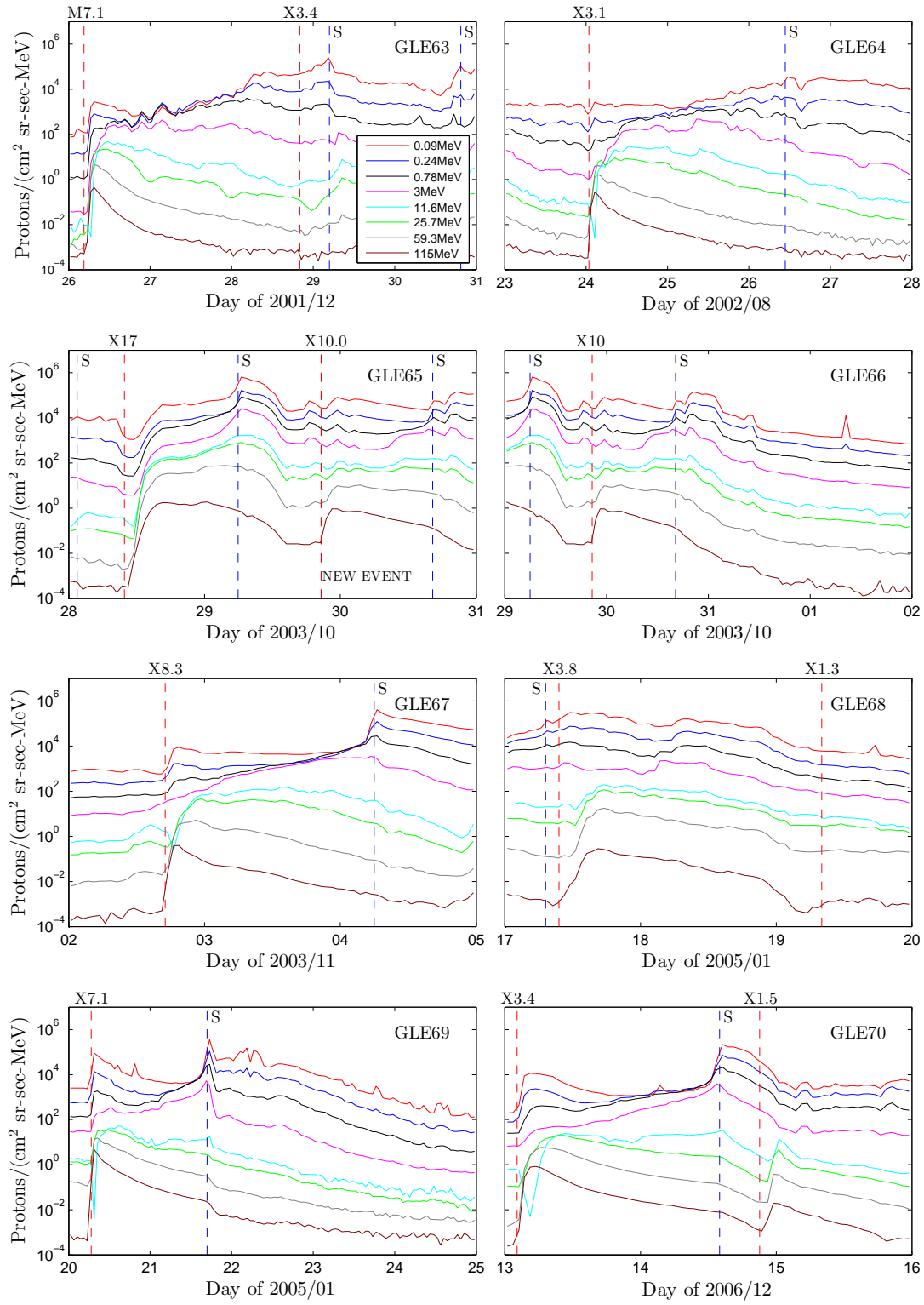


**Figure 2.** Similar as Figure 1 except for GLE63 to GLE70.

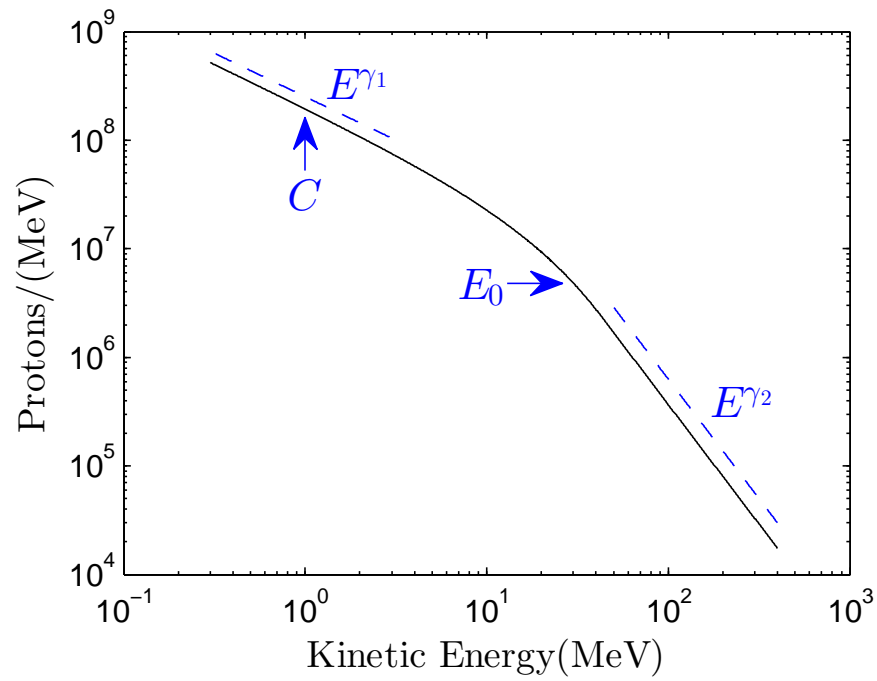


**Figure 3.** A typical double power-law energy spectrum with the four spectral parameters.

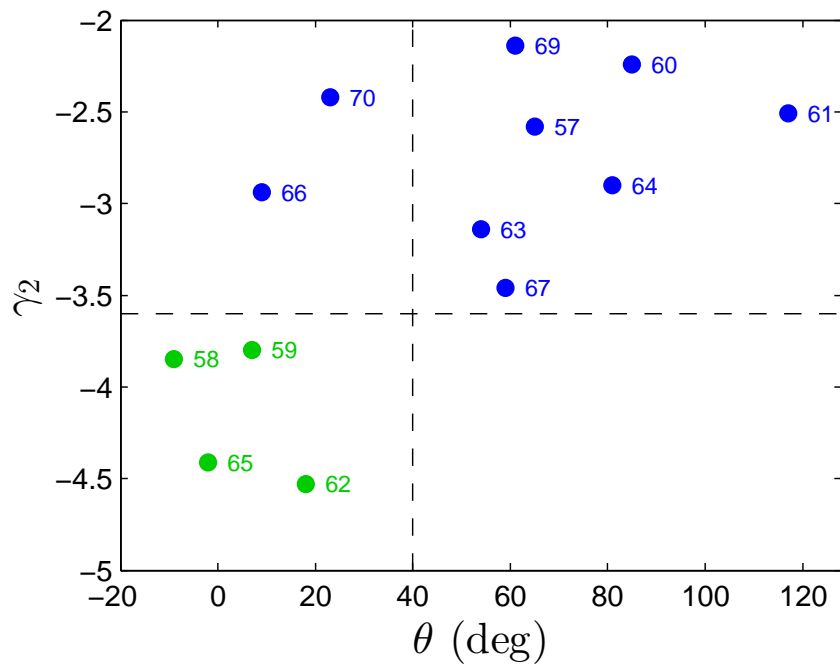


**Figure 4.** The high-energy power-law slope  $\gamma_2$  are plotted versus flare longitude  $\theta$ , and the numbers in the figure indicate the GLE number.



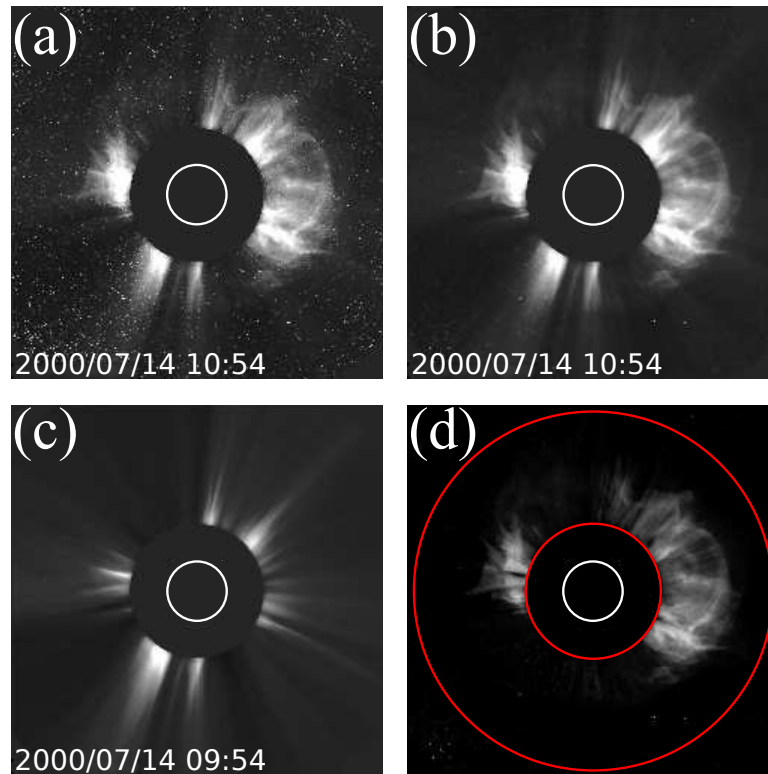


**Figure 5.** The CME images for GLE59. Panel (a) shows the CME image that has been converted to gray image, and the observation is from LASCO/C2 field of view; Panel (b) is similar as panel (a) except that the noise is removed; Panel (c) shows the pre-event image with noise removed; Panel (d) shows the pure CME by making a difference between panel (b) and panel (c).

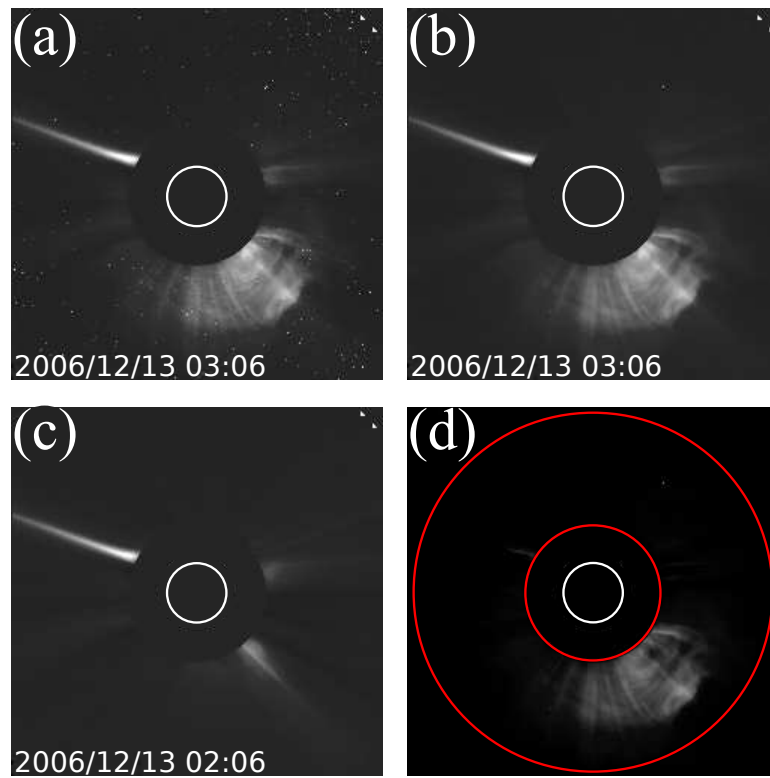


**Figure 6.** The same as Figure 5 except that the event is GLE70.

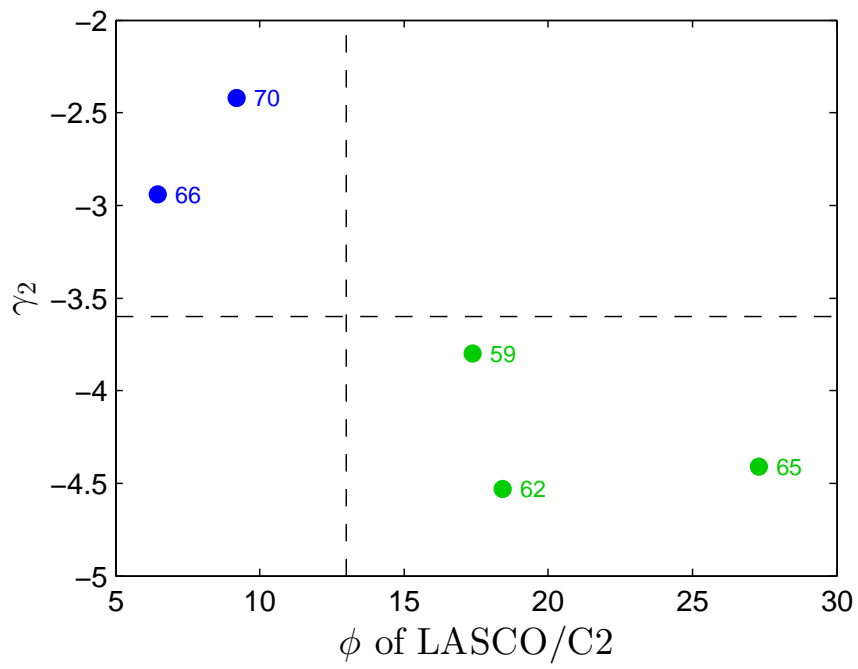


**Figure 7.** The high-energy power-law slope  $\gamma_2$  as a function of the brightness  $\phi$  of CME image of the blue and green events with  $\theta \leq \theta_f$ .

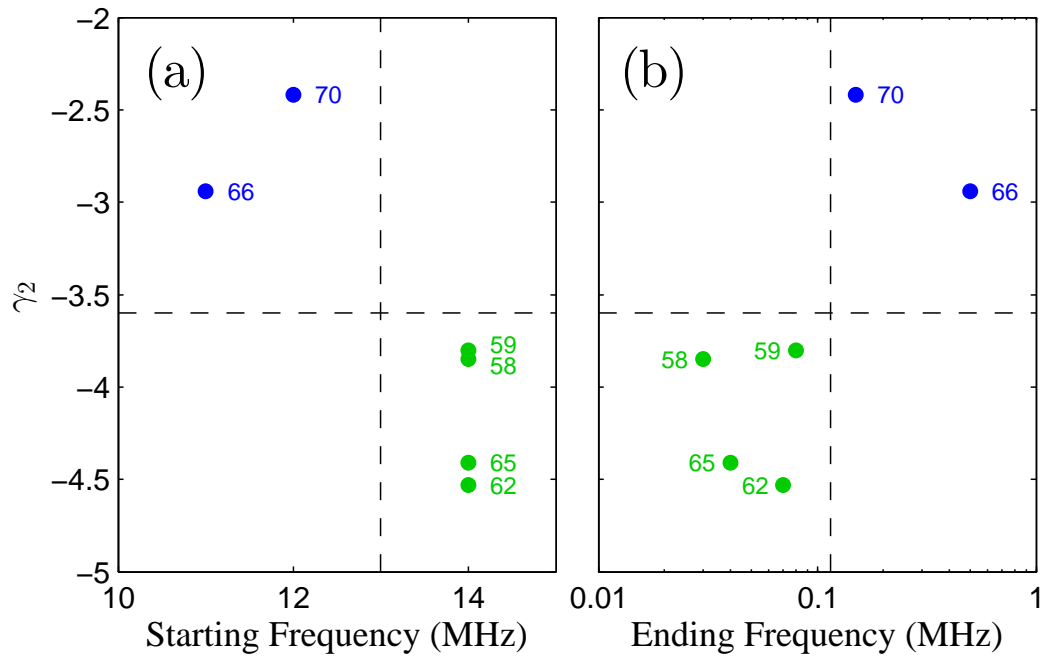


**Figure 8.** The high-energy power-law slope  $\gamma_2$  as a function of the starting and ending frequencies of DH type II radio bursts in left and right panels, respectively, for blue and green events with  $\theta \leq \theta_r$ . Note that in panel (a) the starting frequencies of the green events are greater than or equal to 14 MHz.

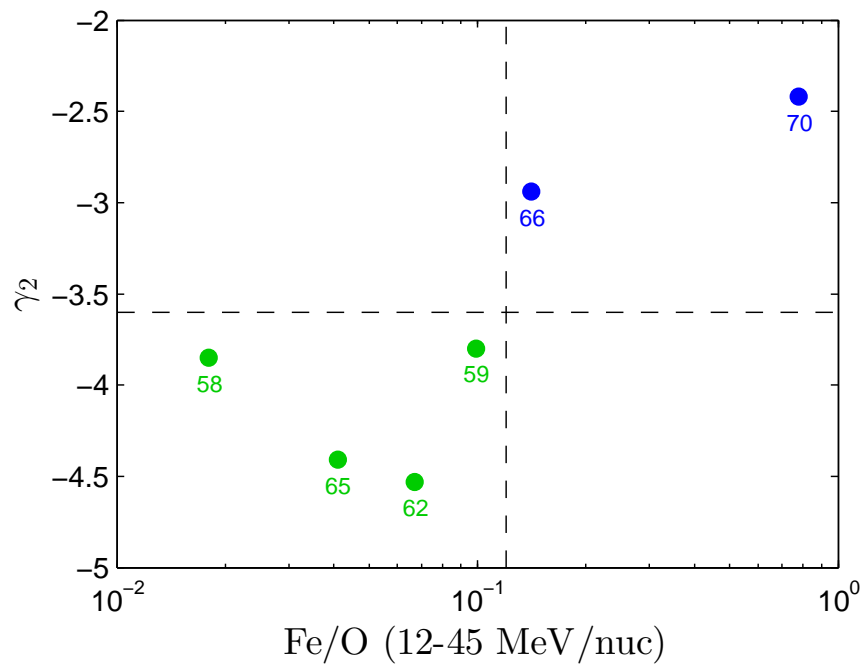


**Figure 9.** The high-energy power-law slope  $\gamma_2$  as a function of the 12–45 MeV/nuc Fe/O ratio measured by ACE/SIS for blue and green events with  $\theta \leq \theta_t$ .

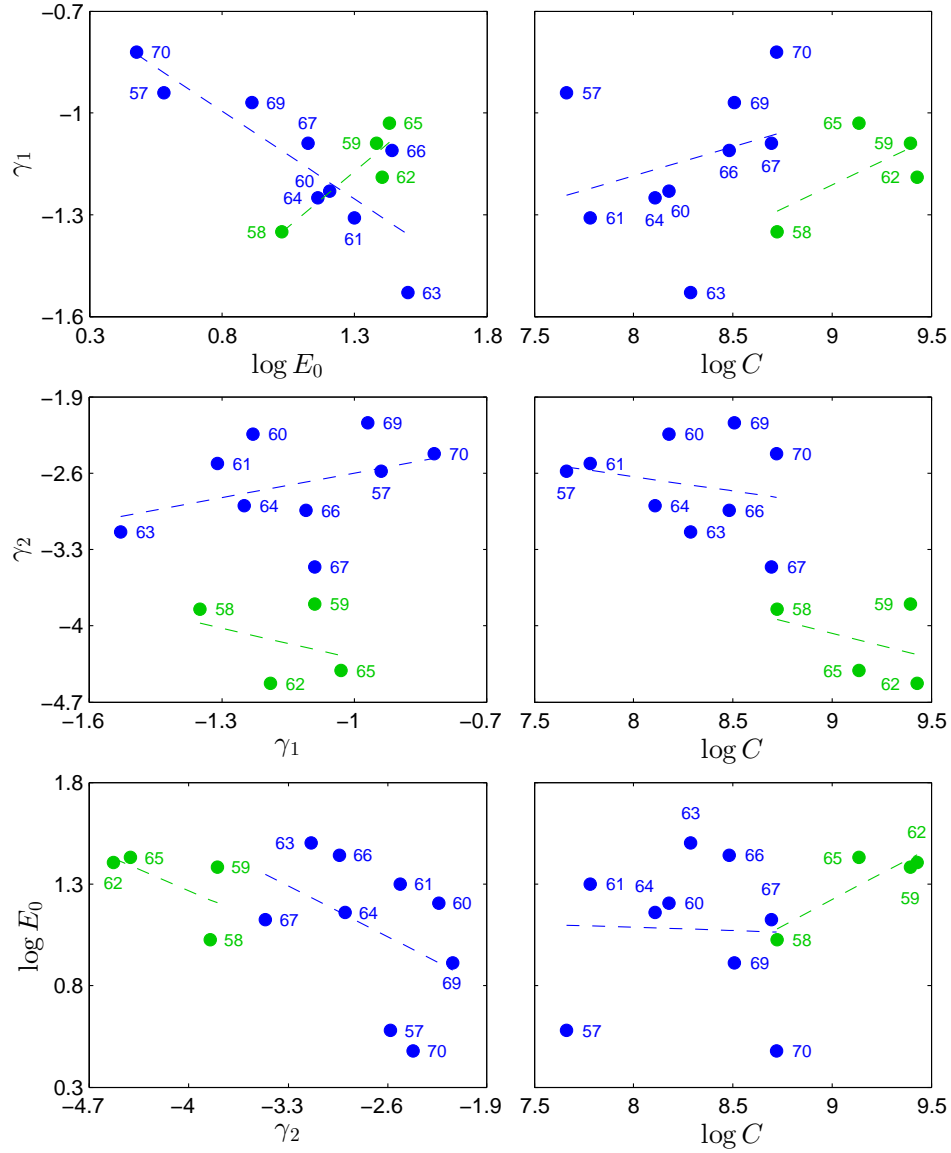


**Figure 10.** The correlations of the four spectral parameters with each other. Blue and green indicate the blue and green events, respectively. Dashed lines indicate the linear fitting.

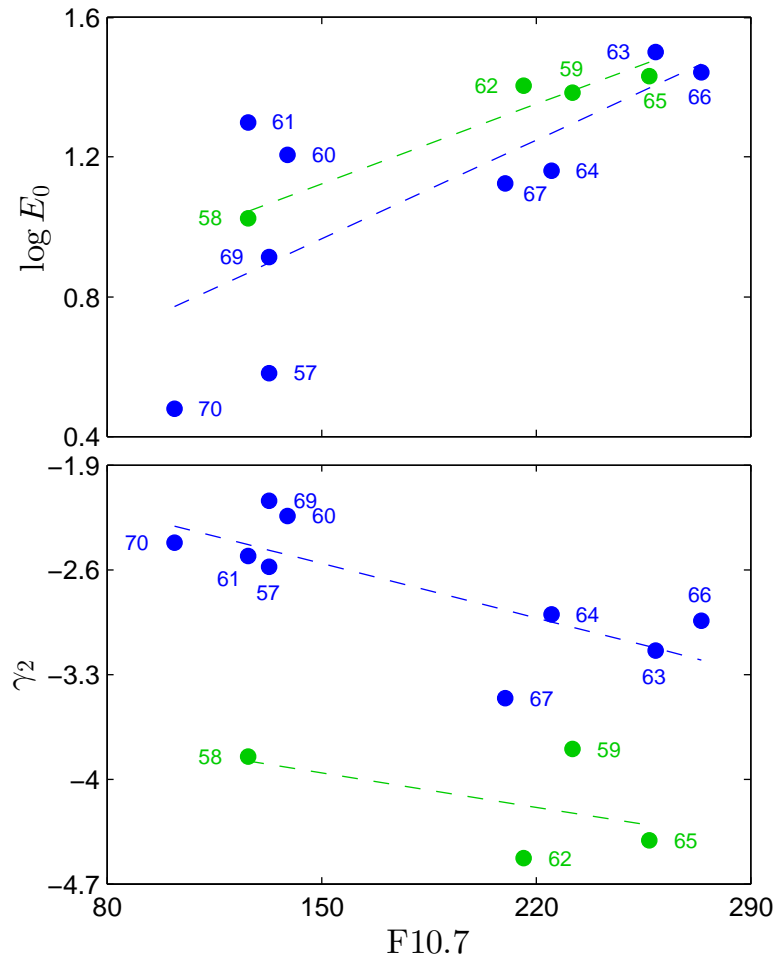


**Figure 11.** Two spectral parameters,  $\log E_0$  and  $\gamma_2$  as function of the solar activity index  $F_{10.7}$  in the upper and lower panels, respectively.

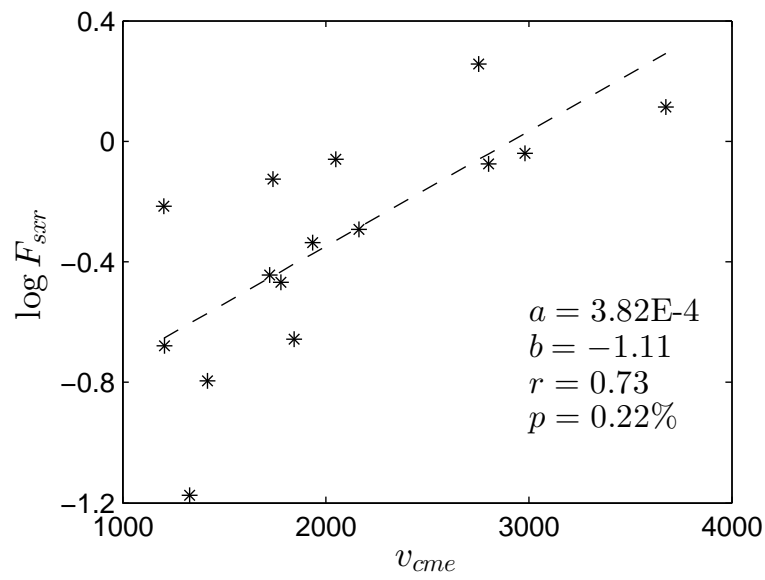


**Figure 12.** The integral soft X-ray flux of all of the GLEs except GLE61 during solar cycle 23,  $\log F_{sxr}$ , as a function of the space speed of CMEs, which are from *Gopalswamy et al.* [2012]. The black dashed line indicates linear fitting. It is noted that  $a$ ,  $b$  are regression parameters and  $r$ ,  $p$  are correlation coefficient and the level of statistical significance, respectively.



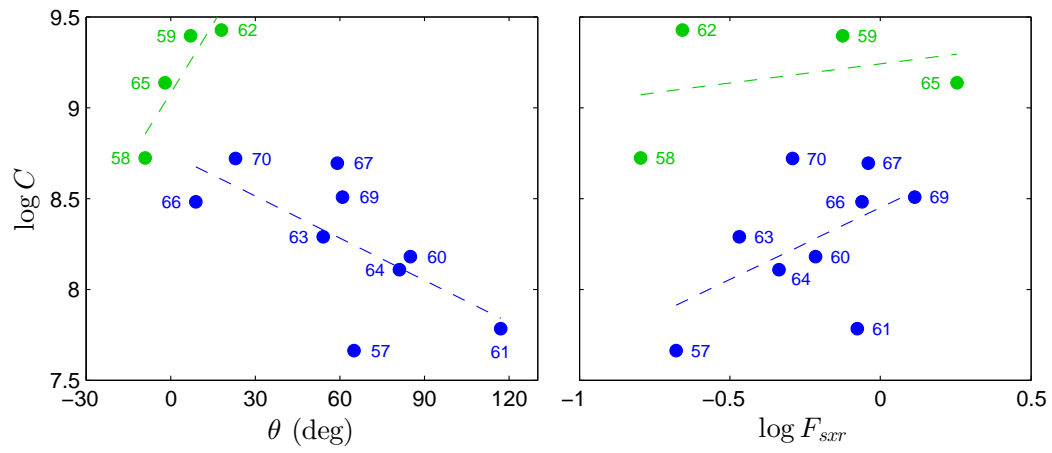


**Figure 13.** Spectral parameter,  $\log C$ , is plotted versus  $\theta$  and  $\log F_{sxr}$  in the left and right panels, respectively.

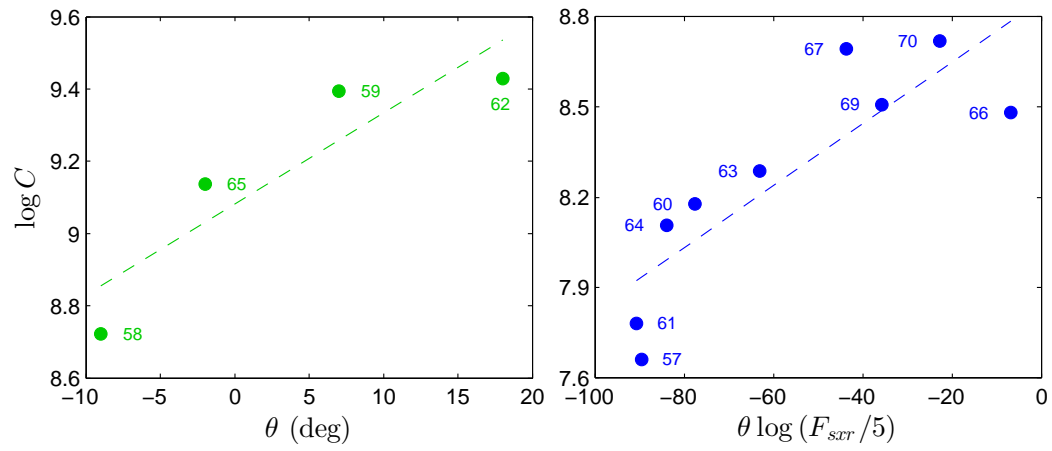


**Figure 14.** Spectral parameter,  $\log C$ , is plotted as a function of  $\theta$  in the left panel for green events, while  $\log C$  of blue events is plotted as a function of  $\theta \log(F_{sxr}/5)$  in the right panel.

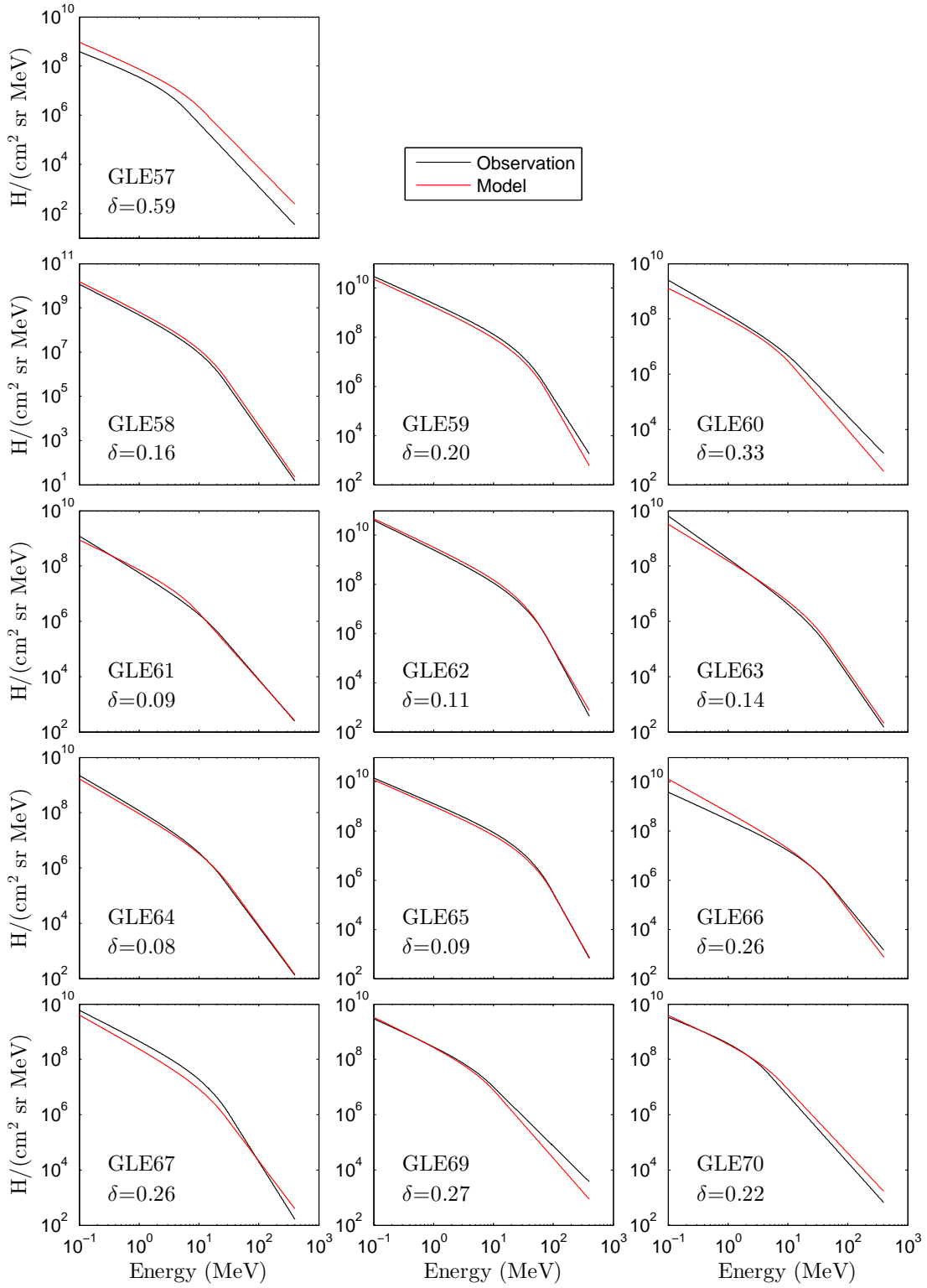


**Figure 15.** Energy spectra from observation and model in black and red, respectively, for 13 GLEs during solar cycle 23.  $\delta$  is calculated with equation (6).

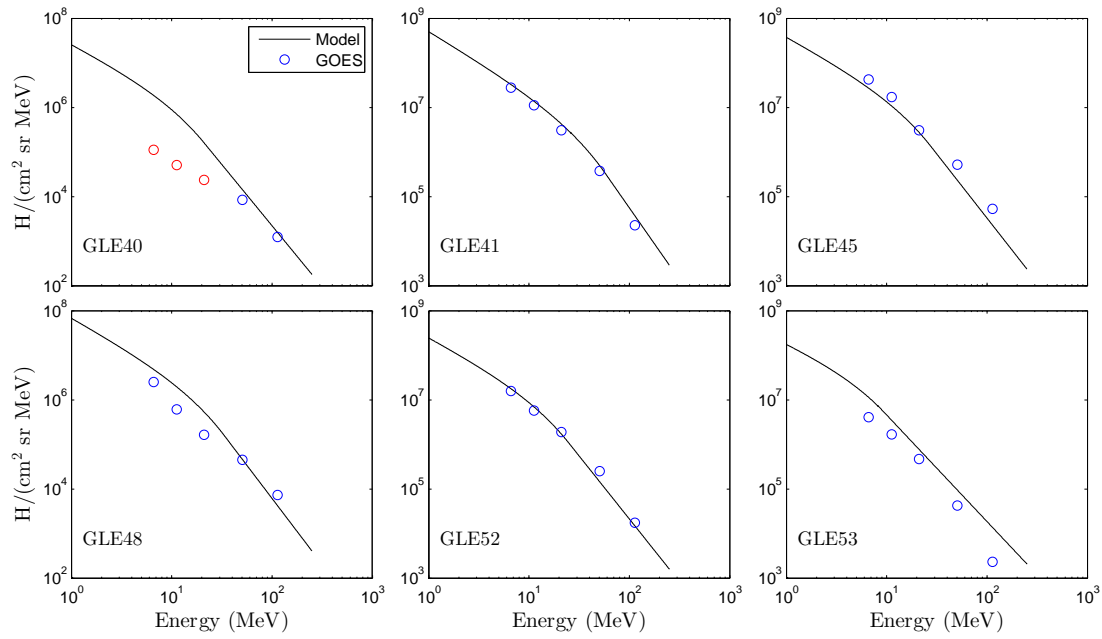


**Figure 16.** The energy spectra from the model are compared with the observations for six GLEs of solar cycle 22, and the observations are from GOES-7 differential channels (channels P2–P6). The red color indicates the data points are influenced by some effects.

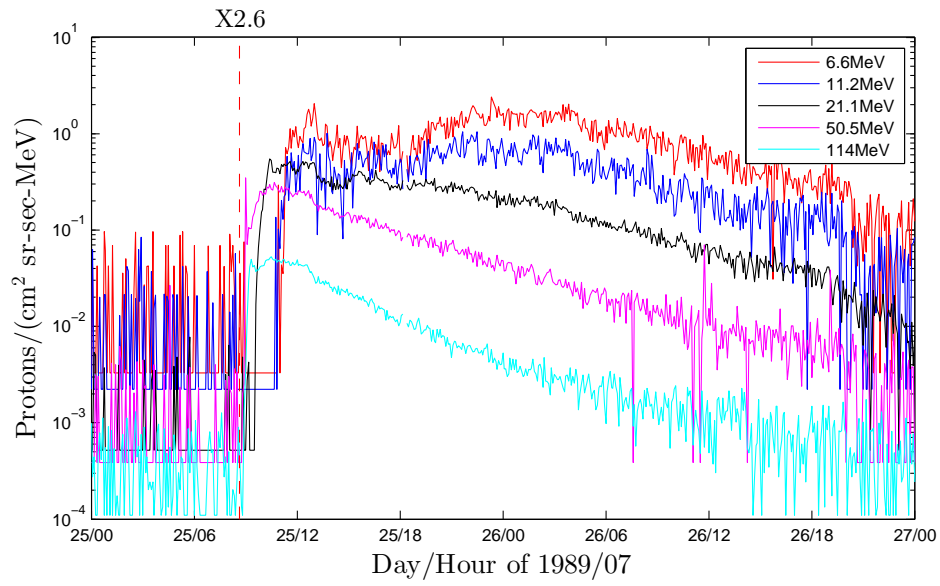


**Figure 17.** Proton intensity-time profiles for GLE40, and the intensities of relatively low energy protons are suppressed to some degree.

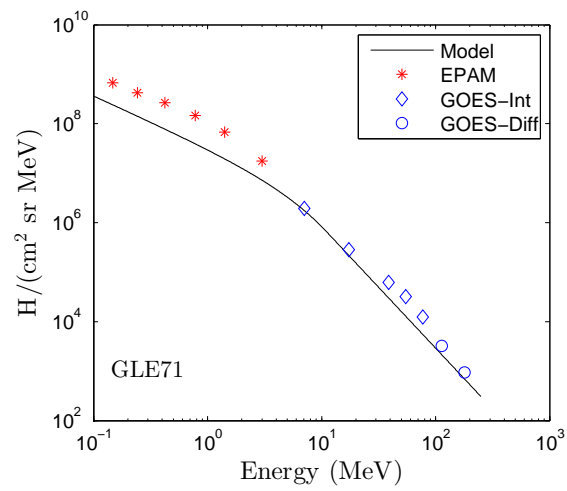


**Figure 18.** The energy spectrum from the model are compared with the observations for GLE71 of solar cycle 24, and the observations are from ACE/EPAM and GOES-13 differential channels (channels P6–P7) and integral channels ( $> 5$ ,  $> 10$ ,  $> 30$ ,  $> 50$ ,  $> 60$ , and  $> 100$  MeV). The red color indicates the data points are influenced by some effects.

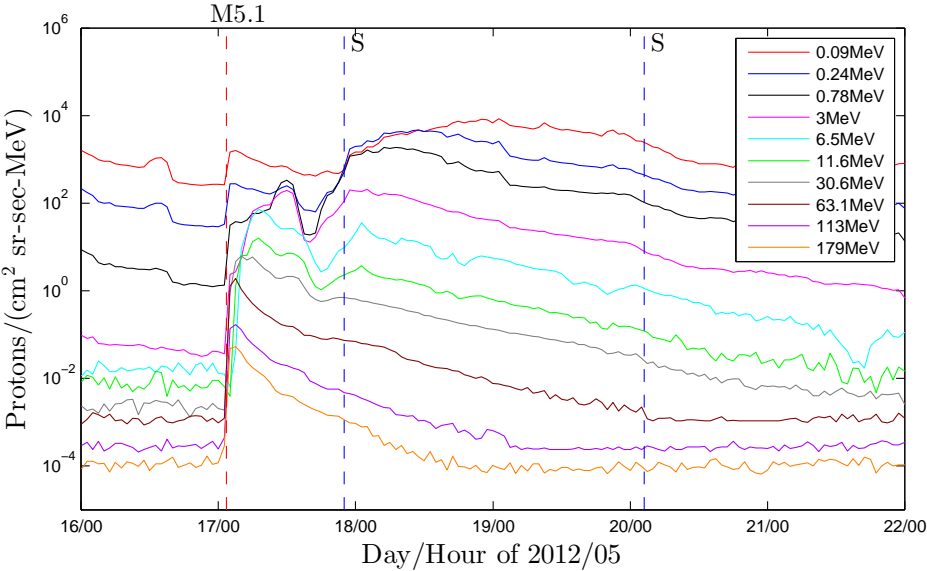


**Figure 19.** Proton intensity-time profiles for GLE71.

**Table 1.** Some related parameters of solar cycle 23 GLEs.

GLE #	Date	Location	$\theta \leq \theta_t$	Category	$\phi$	$f_{start}$ (MHz)	$f_{end}$ (MHz)	Fe/O 12–45 MeV/n	$F_{10.7}$ (sfu)	$F_{sxr}$ (W/m <sup>2</sup> )	$v_{cme}$ (km/s)
55 <sup>a</sup>	11/06/97	S18W63							114	0.360 <sup>b</sup>	1726
56 <sup>a</sup>	05/02/98	S15W15							113	0.067	1332
57	05/06/98	S11W65	N	blue					133	0.210	1208
58	08/24/98	N35E09	Y	green		14	0.03	0.018±0.001	126	0.160	1420 <sup>d</sup>
59	07/14/00	N22W07	Y	green	17.39	14	0.08	0.099±0.010	232	0.750	1741
60	04/15/01	S20W85	N	blue					139	0.610	1203
61	04/18/01	S23W117	N	blue					126	0.838 <sup>c</sup>	2712
62	11/04/01	N06W18	Y	green	18.43	14	0.07	0.067±0.007	216	0.220	1846
63	12/26/01	N08W54	N	blue					259	0.340	1779
64	08/24/02	S02W81	N	blue					225	0.460	1937
65	10/28/03	S20E02	Y	green	27.30	14	0.04	0.041±0.004	257	1.800	2754
66	10/29/03	S19W09	Y	blue	06.46	11	0.50	0.141±0.007	274	0.870	2049
67	11/02/03	S18W59	N	blue					210	0.910	2981
68 <sup>a</sup>	01/17/05	N14W25							145	0.840	2802
69	01/20/05	N14W61	N	blue					133	1.300	3675
70	12/13/06	S06W23	Y	blue	09.20	12	0.15	0.778±0.016	102	0.510	2164

<sup>a</sup> The events are excluded for statistical analysis.

<sup>b</sup> 0.036 W/m<sup>2</sup> from SWPC, but we use 0.36 W/m<sup>2</sup> according to our calculation from GOES-9 soft X-ray flux.

<sup>c</sup> It is not actual value but derived from the correlation that is presented in Figure 12.

<sup>d</sup> The value is derived from ICME observations and ESA model [Gopalswamy *et al.*, 2012].



**Table 2.** The regression parameters ( $a$ ,  $b$ ), the correlation coefficients ( $r$ ), and the level of statistical significance ( $p$ ) of linear fittings for the two types of events.

Parameters		Blue events				Green events			
$x$	$y$	$a$	$b$	$r$	$p$	$a$	$b$	$r$	$p$
$\log E_0$	$\gamma_1$	-0.519	-0.579	-0.86	0.30%	0.655	-2.02	0.90	10%
$\log C$	$\gamma_1$	0.171	-2.55	0.30	44%	0.278	-3.71	0.65	35%
$\gamma_1$	$\gamma_2$	0.754	-1.84	0.38	32%	-0.934	-5.24	-0.35	65%
$\log C$	$\gamma_2$	-0.263	-0.528	-0.23	56%	-0.456	0.0307	-0.40	61%
$\gamma_2$	$\log E_0$	-0.357	0.113	-0.44	24%	-0.300	0.0687	-0.59	41%
$\log C$	$\log E_0$	-0.0319	1.34	-0.034	93%	0.516	-3.42	0.88	12%
$F_{10.7}$	$\log E_0$	0.00404	0.360	0.73	2.6%	0.00326	0.634	0.97	3.0%
$F_{10.7}$	$\gamma_2$	-0.00521	-1.78	-0.77	1.6%	-0.00327	-3.47	-0.50	50%
$\theta$	$\log C$	-0.00772	8.74	-0.66	5.1%	0.0252	9.08	0.90	9.7%
$\log F_{sxr}$	$\log C$	0.790	8.45	0.52	16%	0.213	9.24	0.32	68%
$\theta \log (F_{sxr}/5)$	$\log C$	0.0103	8.86	0.85	0.40%				

**Table 3.** Some key parameters of solar cycles 22 and 24 GLEs.

GLE #	Solar Cycle #	Date	Location	$F_{10.7}$ (sfu)	$F_{sxf}$ <sup>a</sup> (W/m <sup>2</sup> )
40	22	25/07/89	N25W84	186	0.115
41	22	16/08/89	S18W84	278	3.451
45	22	24/10/89	S30W57	211	1.842
48	22	24/05/90	N33W78	228	0.282
52	22	15/06/91	N33W69	201	1.211
53	22	25/06/92	N09W67	118	0.801
71	24	17/05/12	N11W76	131	0.099

<sup>a</sup> The values are obtained from GOES-7 soft X-ray flux for GLEs during solar cycle 22. For GLE71, the value is from SWPC.